scientific reports

Check for updates

OPEN

Characterization of fully-evaporated perovskite solar cells and photodetectors under high-intensity pulsed proton irradiation

Hryhorii P. Parkhomenko[1], Andriy I. Mostovyi[1], Marat Kaikanov[1], Jessica Strey[2], Mircea C. Turcu[2], Marvin Diederich[2], Sascha J. Wolter[2], Verena Steckenreiter[2], Joachim Vollbrecht[2]✉ & Viktor V. Brus[1]✉

This study investigates the impact of proton irradiation on perovskite devices fabricated fully through vacuum deposition. Exposure to irradiation induces changes in both electrical and optical properties. The analysis reveals that the main factors influencing the observed performance changes in solar cells are a significant reduction in shunt resistance and a minor increase in series resistance, with minimal alterations in recombination dynamics. Remarkably, the devices maintain promising photodetector characteristics both before and after proton irradiation, particularly in a self-powered mode without a reverse bias. These findings provide valuable insights into the resilience of vacuum-deposited perovskite devices against ionizing radiation, highlighting their potential for applications in radiation-prone environments, such as the nuclear industry or space exploration.

Keywords Perovskite solar cells, Perovskite photodetector, Radiation hardness, Proton irradiation, Recombination dynamics

In recent years, the field of hybrid inorganic–organic photovoltaic devices has witnessed remarkable advancements, particularly in the realm of active layers based on perovskites[1–4]. These developments have led to notable achievements, with independently reported power conversion efficiencies surpassing $\eta = 26.1\%$ in single-junction perovskite solar cells (PSCs) and the efforts to combine the advantages of PSCs with those exhibited by silicon solar cells resulted in perovskite/Si-tandem devices with record-breaking efficiencies ($\eta = 33.9\%$)[5]. However, the quest for high efficiencies is not the sole focus of current PSC research; it has also extended to encompass other critical areas: reproducibility, long-term stability, and the facilitation of large-area deposition techniques[6–12].

In parallel with these endeavors, the utilization of perovskites as active layers in various optoelectronic devices has garnered significant attention in the recent years. Applications such as light-emitting diodes (LEDs) and photodetectors (PDs) have emerged as notable use-cases[13–15]. In photodetectors, specific device attributes have assumed paramount importance, including the capability to detect photons across a defined wavelength range over several orders of magnitude of illumination intensities and the operational speeds of the devices[16,17]. Additionally, the ability to withstand environmental stressors has become a crucial consideration for PD applications. Particularly noteworthy is the suitability of perovskite materials for scenarios necessitating enhanced radiation hardness, such as in the nuclear industry or space exploration[18–21].

The latter example has recently been in the spotlight, since deposition of perovskite materials, along with other essential layers such as transport layers and metal electrodes, can be effectively achieved through evaporation techniques[22,23]. This method not only offers precise control over layer deposition but also presents a compelling advantage for in-situ device fabrication in space applications. The vacuum conditions required for evaporation, though costly on Earth, naturally align with the vacuum conditions prevalent in the space environment, making this fabrication approach a preferred choice for advancing PSC and PD technology in space[24–27].

[1]Department of Physics, School of Sciences and Humanities, Nazarbayev University, Astana 010000, Republic of Kazakhstan. [2]Department of Photovoltaics, Institute for Solar Energy Research Hamelin, 31860 Emmerthal, Germany. ✉email: vollbrecht@isfh.de; vvbrus@gmail.com

In particular, the atmospheric pressure at the Kármán line (100 km altitude) drops to $p \approx 10^{-4}$ mbar and at low Earth orbit (500 km altitude) to $p \approx 10^{-10}$–10^{-8} mbar; as a point of reference, the highest pressure still considered to be ultra-high vacuum is $p = 10^{-9}$ mbar, which is orders of magnitude below the processing pressures for most evaporation techniques[28–30].

In this study, we employed a complete vacuum deposition process to fabricate methylammonium lead triiodide ($CH_3NH_3PbI_3$; MAPI) based perovskite devices featuring the layer sequence glass/ITO/spiro-TTB/$CH_3NH_3PbI_3$/C60/BCP/Cu (cf. Fig. 1, ESI). As the initial operational characteristics, values up to an open-circuit voltage $V_{OC} = 1131.66$ mV, short-circuit current density $J_{SC} = 21.56$ mA cm^{-2}, fill factor $FF = 75.99\%$, and power conversion efficiency $\eta = 17.27\%$ were achieved; further details are described in Table 1 and Fig. S1. Following this, the devices underwent irradiation with protons via three short pulses (150 ns) of 2×10^{12} p cm^{-2}, at an energy of 140 keV, imparting a total fluence of 6×10^{12} p cm^{-2}. As a point of reference, a fluence of 10^{13} p cm^{-2} is usually accumulated over a duration of roughly 30 years at low Earth orbit outside the Van-Allen belts[31]. Subsequent to proton irradiation, comprehensive assessments of the devices as both solar cells and photodetectors were conducted, facilitating a thorough comparison of their performance before and after exposure to ionizing radiation (cf. ESI).

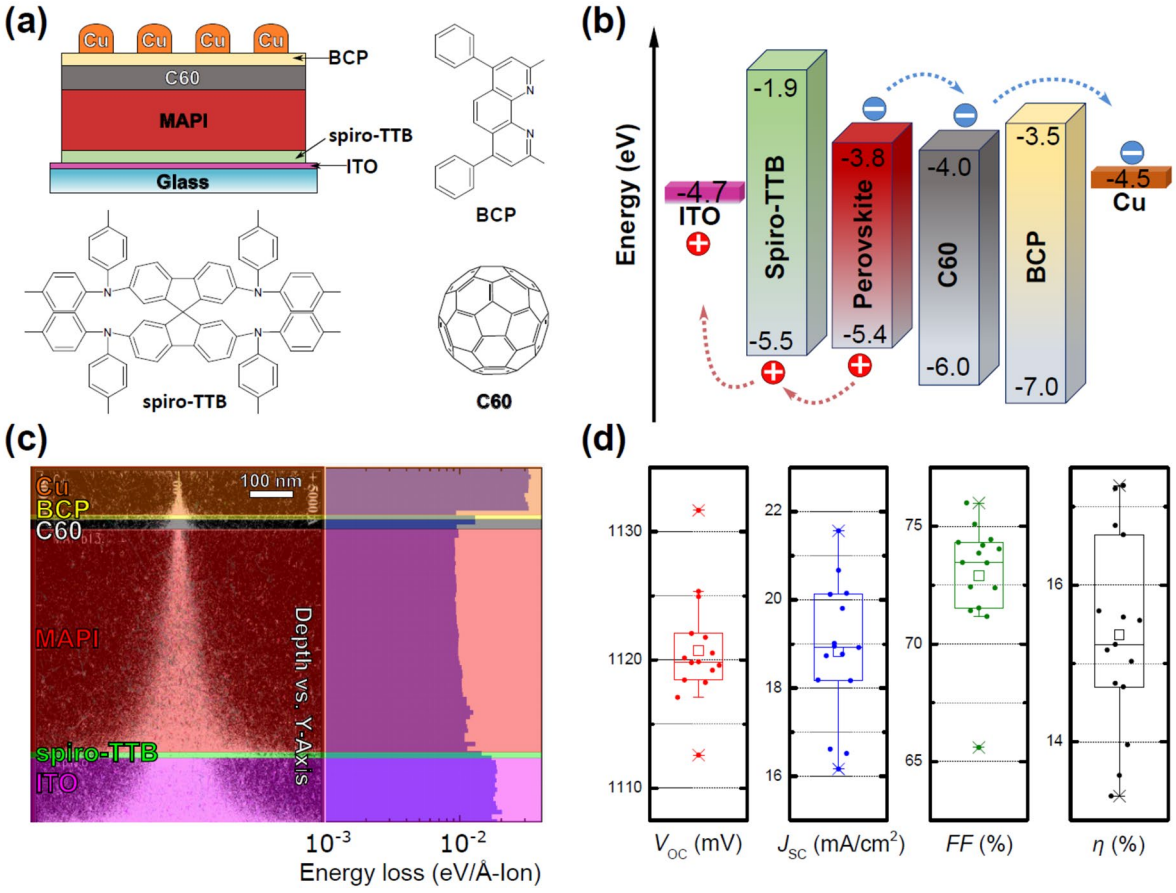

Figure 1. (**a**) Schematic depiction, chemical structures, (**b**) energy levels, and (**c**) SRIM simulations of the studied MAPI devices. (**d**) Initial open-circuit voltage (V_{OC}), short-circuit current density (J_{SC}), fill factor (FF), and power conversion efficiency (η) of the tested solar cells ($n = 15$).

Sample	V_{OC} [mV]	J_{SC} [mA cm^{-2}]	FF [%]	η [%]
Initially*	1120.75 ± 4.29 (1131.66)	18.82 ± 1.55 (21.56)	72.89 ± 2.45 (75.99)	15.36 ± 1.55 (17.27)
Before irradiation	1078.11	17.17	72.38	13.43
After irradiation	1055.77	12.00	56.36	7.14

Table 1. Photovoltaic parameters obtained from the J–V-characteristics of the tested devices. *Average values of 15 tested devices and their standard deviation, maximum values listed in brackets (cf. Fig. S1).

Results and discussion

The damage profile and penetration depth of protons in the device were determined using stopping and range ion modeling (SRIM) utilizing experimentally measured thicknesses and densities of functional layers taken from the literature[32,33] and SRIM libraries. Protons with an energy of 140 keV penetrate all functional layers of the device with decent energy losses for recoils (cf. Fig. 1c), indicating optimal conditions for testing radiation resistance[34,35]. Damage to the functional layers (ETL, HTL, metal, and transparent electrode) will primarily impact the series resistance of the devices, as the resistance of the layers may increase during the irradiation process[19]. The alterations induced by proton irradiation in the perovskite active layer are crucial since the generation-recombination processes occurring in the active layer play a pivotal role in the operation of optoelectronic devices[36–38].

Our study entails a thorough examination of device performance before and after exposure to irradiation. Two key parameters are the cornerstone of the subsequent analyses: the light intensity-dependent voltage–current–density (*J*–*V*) characteristics and the external quantum efficiency (*EQE*). These metrics are crucial for assessing the functionality of the devices, particularly in PSC and PD applications.

The photovoltaic parameters derived from the *J*–*V*-characteristics measured initially after fabrication, directly before irradiation, and directly after irradiation are listed in Table 1. It should be noted that the behavior of the *J*–*V* curves of perovskite optoelectronic devices is dependent on the architecture of the device, pre-bias conditions, and pre-conditioning cycles[39,40]. In the present case, the *J*–*V*-characteristics were measured without the use of pre-bias and pre-conditioning cycles. The reduction between the initial testing of the newly fabricated devices and before irradiation can be linked to performance losses resulting from transporting the devices across continents.

A relatively small reduction in V_{OC} as well as more significant reductions in J_{SC} and *FF* can be observed after the tested devices have been subjected to the irradiation treatment. Unsurprisingly, the latter two parameters are the main reason for the reduction of the power conversion efficiency from $\eta = 13.43\%$ to $\eta = 7.14\%$.

The *J*–*V*-characteristics were measured across a broad range of light intensities, providing foundational data for in-depth device evaluation and subsequent intricate analyses of device behavior (cf. Fig. 2). Even when subjected to low illumination intensities, we observed that the changes in current density at reverse and low forward biases remained relatively small, suggesting that the devices exhibited stability under these conditions. However, a notably different behavior in the current–density profile became apparent after irradiation. Specifically, we observed a more pronounced bias-dependent increase in the absolute value of current density at low illumination intensities.

The external quantum efficiency (*EQE*) measurements of the devices were essential in understanding their response to irradiation, particularly in the context of their spectral sensitivity (cf. Fig. 2). Prior to irradiation, the *EQE* measurements showed increased values in the wavelength region of $\lambda = 350$–600 nm when a reverse bias was applied. After irradiation, the *EQE* landscape exhibited significant changes. Notably, there was a reduction in *EQE*, primarily in long wavelength ranges ($\lambda = 500$–750 nm). Intriguingly, the bias-driven increase in *EQE* observed before irradiation in the $\lambda = 350$–600 nm range was less pronounced post-irradiation, with the remaining bias-driven enhancement being now primarily centered in the $\lambda = 500$–750 nm range.

The observed changes in the *J*–*V*-characteristics and *EQE* provide valuable insights into the impact of irradiation on the devices' performance. The increase in current density after irradiation suggests alterations in the electrical properties of the device, which may be attributed to irradiation-induced defects or changes in carrier mobility. The reduction in *EQE* at longer wavelengths after irradiation could indicate a shift in the absorption properties of the devices, possibly due to structural modifications caused by irradiation. The change in *EQE* enhancement from the $\lambda = 350$–600 nm range to the $\lambda = 500$–750 nm range suggests a spectral reconfiguration of the sensitivity of the devices.

Solar cells

A more advanced analysis of the tested devices as PSCs is based on the qualitative and quantitative analysis of the recombination dynamics before and after irradiation. The qualitative analysis is spear headed by the characterization of the light intensity dependent J_{SC} and V_{OC} behavior (cf. Fig. 3)[41–43]. The J_{SC} of the tested devices exhibits a linear relationship over a wide light intensity range in a double-logarithmic plot:

$$J_{SC} = L^{\alpha} \Leftrightarrow log\ J_{SC} = \alpha\ log\ L. \tag{1}$$

The resulting proportionality factor of $\alpha = 0.9834$ and $\alpha = 0.9395$ for the devices before and after irradiation, respectively, are indicative of an increased band-to-band recombination, once the devices were irradiated.

In contrast, the open-circuit voltages exhibit more drastic and significant changes over the tested light intensity range, including even more pronounced differences of the tested devices before and after irradiation. A semi-logarithmic relationship between the V_{OC} and the light intensity is employed to estimate the dominant type of recombination mechanism:

$$V_{OC} \propto S\frac{kT}{q} \cdot \ln L \tag{2}$$

where k is the Boltzmann constant, T is the absolute temperature, q is the elementary charge, and S is a unitless factor that indicates the dominant type of recombination mechanism. Dominant band-to-band recombination yields $S = 1$, bulk-trap assisted recombination leads to $S > 1$, whereas surface-trap assisted recombination results in $S < 1$[44–47]. The devices before irradiation tend to yield a linear behavior in the semi-logarithmic plot, whereas the irradiated devices exhibit non-linear properties, specifically at lower light intensities. This latter

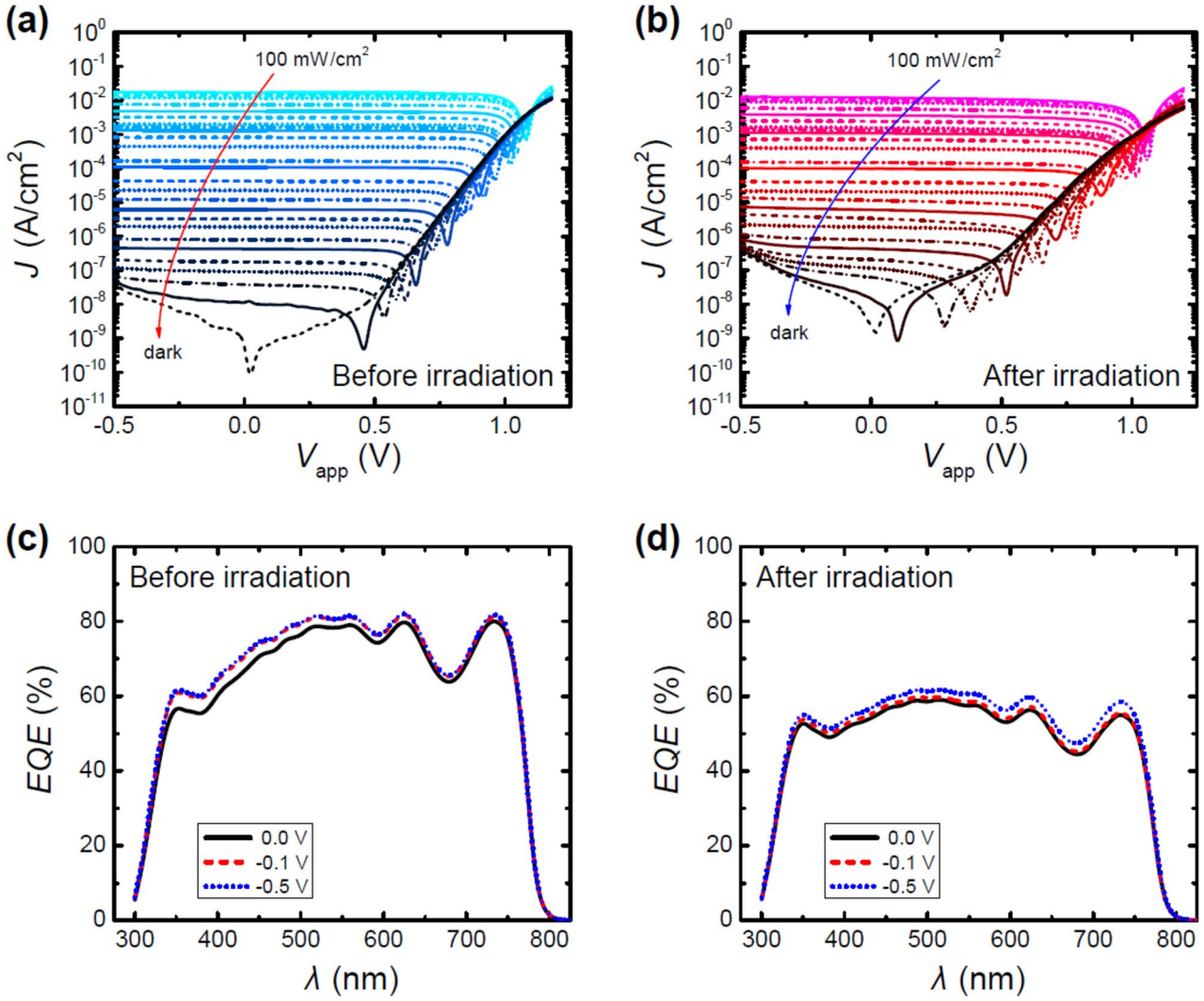

Figure 2. (**a**,**b**) Light intensity dependent *J*–*V*-characteristics of the tested devices before and after irradiation. (**c**,**d**) External quantum efficiency at different applied voltages of the tested devices before and after irradiation.

observation is likely linked with a reduced shunt resistance R_{sh} of the irradiated devices, which usually result in non-linear behavior of the V_{OC} at low light intensities. This is verified by the determination of the differential resistance ($R_{diff} = dI/dV$) based on the *I*-*V*-curves in the dark. At high forward bias, the differential resistance can be assumed to be equal to the series resistance R_s, whereas the shunt resistance R_{sh} can be estimated from the differential resistance at an applied voltage of $V_{app} = 0$ V[48]. Indeed, a significant reduction of the shunt resistance can be observed, once the tested PSCs were irradiated, namely from $R_{sh} = 509$ MΩ to $R_{sh} = 94$ MΩ. Conversely, an increased series resistance was exhibited by the tested devices, once they were irradiated, namely from $R_s = 79.3$ Ω to $R_s = 197.2$ Ω, respectively.

Nonetheless, the evaluation of the slope factor *S* in the linear parts of the V_{OC}–ln*L*-plot reveals that the recombination dynamics is predominantly band-to-band recombination, regardless of whether the PSCs were irradiated or not. However, the possibility exists that the impact of bulk and surface trap-assisted recombination contributions might counterbalance each other, resulting in slopes close to $1kT/q$[49,50]. Therefore, it was necessary to perform more elaborate experiments to elucidate quantitatively the recombination dynamics of these devices. A combination of open-circuit-voltage-decay (OCVD) and impedance spectroscopy (IS) measurements yielded important insights regarding precisely the quantitative recombination dynamics. The transient nature of the OCVD technique facilitated the observation of the voltage changes of the tested device, which is held at open-circuit conditions by employing a high-impedance buffer, after turning off the external illumination source[51]. While OCVD on its own can already provide detailed information regarding the recombination dynamics, its full potential is unlocked, if it is combined with another technique that allows to convert the transient open-circuit voltage $V_{OC}(t)$ into the transient charge carrier density $n_{OC}(t)$[45,46]. In this study, impedance spectroscopy was employed to determine the charge carrier density under open-circuit conditions and the same illumination conditions that were used for the OCVD measurements. Thus, a direct link between the voltage V_{OC} ($t = 0$) and the charge carrier density n_{OC} could be established (cf. Figs. S3 and S4)[48,52–54].

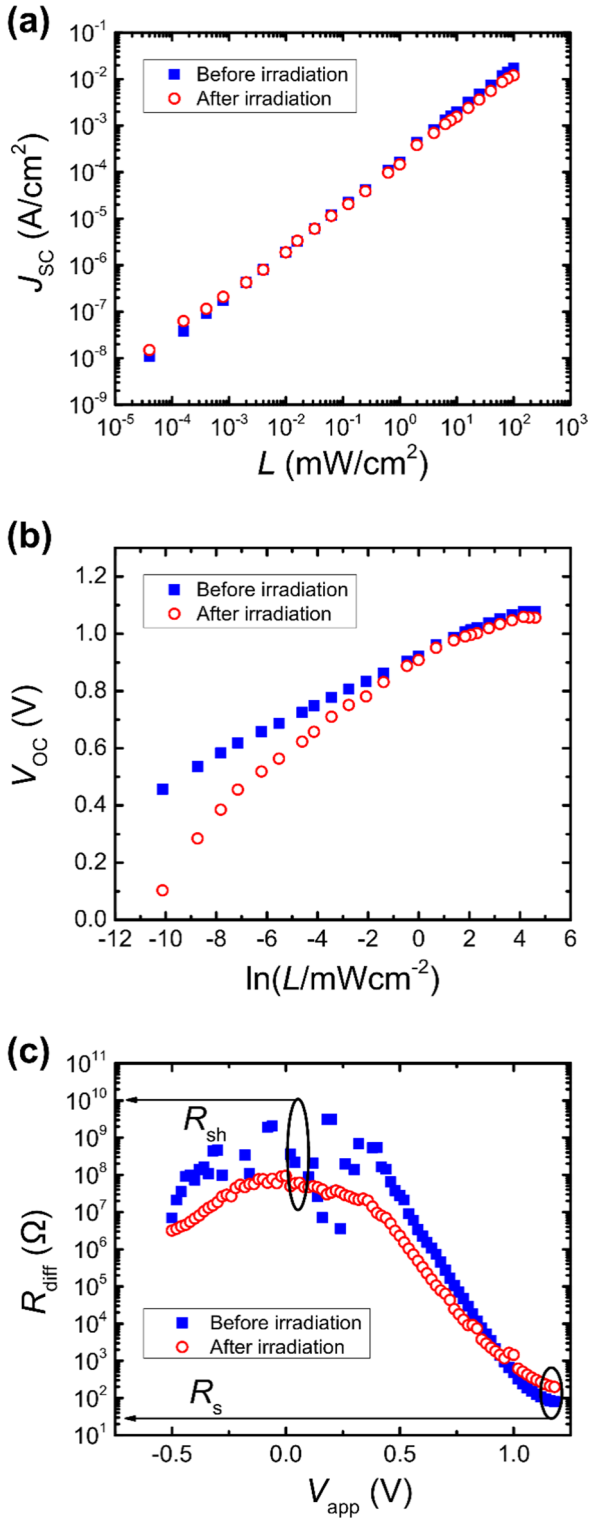

Figure 3. (**a**) Light intensity-dependent short-circuit current density and (**b**) open-circuit voltage of the tested devices before and after irradiation. (**c**) Differential resistance of the tested devices before and after irradiation.

Similar to the qualitative investigation of the recombination dynamics via the light-intensity dependent V_{OC}, three types—first, second, and third order processes—of possible recombination pathways were taken into consideration during the quantitative analysis that is based on the experimental results obtained from OCVD and IS. It is revealed that all aforementioned types of recombination contribute to the total recombination rate (cf. Fig. S5 and Table 2). Interestingly, the irradiation leads to an increase of the first order recombination coefficient by nearly one order of magnitude, namely from $k_1 = 5.69\ s^{-1}$ to $k_1 = 49.81\ s^{-1}$. The band-to-band recombination

Sample	α	S [kT/q]	R_{sh} [MΩ]	R_s [Ω]	k_1 [s^{-1}]	k_2 [$cm^3\ s^{-1}$]	k_3 [s^{-1}]
Before irradiation	0.9834	1.18	509.0	79.3	5.69	1.85×10^{-14}	1.50×10^{-11}
After irradiation	0.9395	1.09	94.4	197.2	49.81	3.26×10^{-14}	1.18×10^{-11}

Table 2. Relevant parameters describing the recombination and loss processes of the tested devices.

also increases after irradiation, as evidenced by the relevant coefficient changing from $k_2 = 1.85\times10^{-14}$ $cm^3{\cdot}s^{-1}$ to $k_2 = 3.26\times10^{-14}$ $cm^3\ s^{-1}$. The contributions from third or pseudo-third order recombination, which in all likelihood are stemming from surface trap-assisted recombination rather than Auger recombination, remain on a similar level before and after irradiation.

Overall, the analysis as PSCs of the tested devices before and after proton irradiation indicates that the main contributing factors for the observed changes in performance are the significant reduction of the shunt resistance R_{sh} and to a lesser extend the increased series resistance R_s. While the qualitative and quantitative analysis of the recombination dynamics revealed some changes upon irradiation, these appear to be only of minor consequence. However, it is known that an increase in charge carrier recombination can result in a reduction in shunt resistance and, accordingly, an increase in the leakage current[55–57]. This increase in leakage currents is responsible for the nonlinear nature of the light intensity-dependent open-circuit voltage discussed above[58]. Furthermore, the decrease in the open-circuit voltage after irradiation may also be due to an increase in recombination losses[20,53]. The observed increase in series resistance of the PSCs subsequent to proton irradiation is primarily attributed to damage to the functional layers (ETL/HTL and/or electrodes)[20,59].

Moreover, the MAPI devices investigated in this study demonstrate pre-irradiation and post-irradiation efficiencies that rank among the highest reported for MAPI devices subjected to analogous irradiation treatments in the existing literature. However, it is noteworthy that perovskite compositions with more intricate structures generally maintain superior efficiencies following proton irradiation of comparable energies and fluences (cf. Table S1).

Photodetectors

The operation of these perovskite devices as photodetectors requires a thorough examination of two aspects that only in part align with the analyses that are usually employed to study PSCs. The first important property that is commonly tested for devices that are used as PDs is the responsivity R. The responsivity of PDs is used as a figure-of-merit that characterizes the ratio of the electrical output in relation to the optical input. In units of ampere produced per watt of incident light, R can be calculated as follows[19]:

$$R = \frac{J_{ph}}{L} = \frac{EQE}{100\%} \cdot \frac{\lambda}{1240\left(nm \cdot W \cdot A^{-1}\right)}, \tag{3}$$

where J_{ph} is the photocurrent density, L is the incident light intensity, λ is the wavelength of the incident light in nanometers, and EQE is the external quantum efficiency. In the case of the tested perovskite devices, it can be seen that the responsivity R before proton irradiation exhibits its maximum of $R = 0.48$ A/W in the region of $\lambda = 750$ nm (cf. Fig. 4). Furthermore, only a small increase of the responsivity R occurs, if a reverse bias is applied. After proton irradiation, a reduction of the responsivity can be observed, most notably in the region of $\lambda = 500$–750 nm, which is directly linked to the changes in the EQE when comparing the devices before and after proton irradiation (cf. Fig. 2). Consequently, only a maximum of $R = 0.35$ A/W can be achieved. Similarly, the irradiated devices also exhibit a more pronounced reverse bias-driven enhancement of the responsivity R in the wavelength range that suffered the most significant responsivity reduction.

The second critical parameter is the linear dynamic range (LDR). This metric characterizes the extent over which the response of the tested PDs exhibits a linear relationship with the incident signal. The LDR, expressed in decibels (dB), can be formally defined and calculated as follows[20]:

$$LDR = 20\ log\frac{L_u}{L_l} = 20\ log\frac{J_u}{J_l}, \tag{4}$$

Here, the variables L_u and L_l represent the upper and lower irradiance levels, respectively. These values delineate the boundaries beyond which deviations from linearity in the signal-irradiance relationship of the PD become noticeable. Consequently, the corresponding photocurrents are denoted as J_u and J_l, respectively.

In the case of the tested perovskite PDs, the linear dynamic range reached values of $LDR = 124$ dB for the device before proton irradiation, without reverse bias as well as with an applied bias of $V_{app} = -0.1$ V. The linear dynamic range decreased to $LDR = 99$ dB, once a stronger reverse bias of $V_{app} = -0.5$ V was applied. A reduction of the LDR was also observed after proton irradiation. This effect was only moderate without any reverse bias ($LDR = 118$ dB), but more pronounced for the cases, where a reverse bias of $V_{app} = -0.1$ V or $V_{app} = -0.5$ V was applied ($LDR = 99$ dB and $LDR = 75$ dB, respectively). The deviation from linearity consistently occurs at lower light intensities across all tested conditions, aligning with the previously discussed behavior of J–V-curves at low light levels. Specifically, this behavior is characterized by an increase in current density attributed to an intensified absolute reverse bias. Hence, this observation is directly linked to the property of the tested devices to act as diodes blocking current flow. Moreover, exposure to proton irradiation led to a further increase in current density within this bias region, which indicates that proton irradiation has a negative impact on the diode characteristics

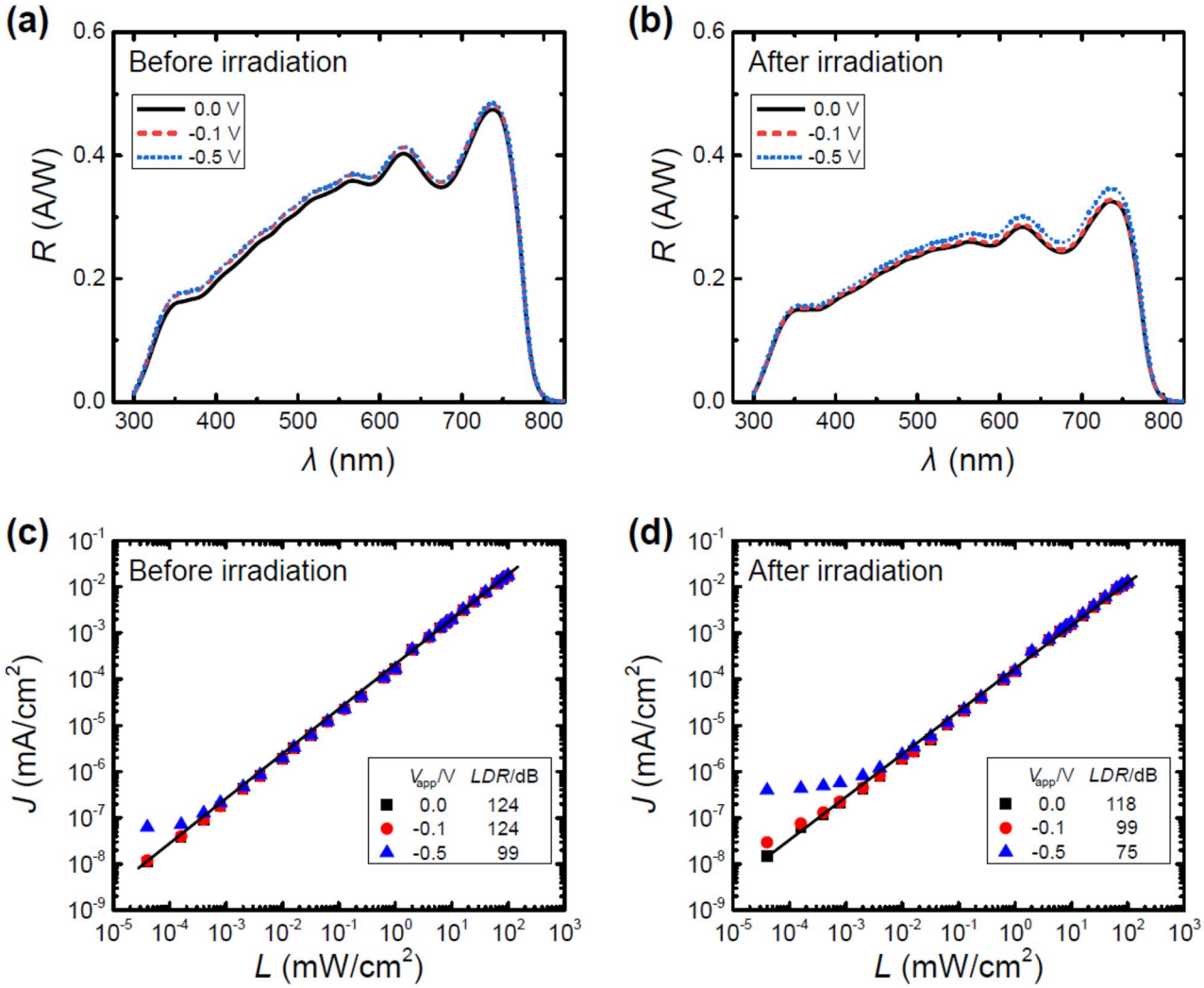

Figure 4. (**a**,**b**) Responsivity at different applied voltages of the tested devices before and after proton irradiation. (**c**,**d**) Determination of the linear dynamic range (*LDR*) at different applied voltages of the tested devices before and after proton irradiation. The solid black line acts as a guide to the eye.

of the tested devices, which agrees with the observed reduction in the shunt resistance R_{sh} discussed previously. In contrast, there were no deviations from linearity at light intensities up to and including $L = 100$ mW cm^{-2}. Under the aforementioned circumstances, the preferred operational mode of the tested PDs is a self-powered one or in other words without the application of a reverse bias.

Another important property of PDs is the characterization of their electrical noise profile, which ultimately is responsible for their detectivity. Specifically in a self-powered mode, two types of noise need to be considered: the current thermal noise $i_{thermal}$, or Johnson noise, and the noise spectral density i_{noise}. Johnson noise is linked to the load resistor, which for the tested devices is equal to the shunt resistance R_{sh}, and independent of frequency. As a result the detectivity limited by Johnson noise D_{th}^{*}, in units of cm·Hz$^{1/2}$/W or Jones, which evaluates the sensitivity to weak optical signals, is used as a figure-of-merit when describing PDs[35,60]:

$$D_{th}^{*} = \frac{R\sqrt{A}}{i_{thermal}} = \frac{R\sqrt{A}}{\sqrt{\frac{2k_B T}{R_{sh}}}}, \tag{5}$$

where R is the responsivity, A is the active device area, k_B is Boltzmann's constant, $i_{thermal}$ is the thermal or Johnson noise, T is the absolute temperature, and R_{sh} is the shunt resistance. The tested devices before proton irradiation exhibit a detectivity of $D_{th}^{*} = 1 \times 10^{13}$–$3 \times 10^{13}$ Jones over a wide spectral range of $\lambda = 350$–750 nm with the highest values at longer wavelengths (cf. Fig. 5). After proton irradiation, the tested devices exhibit decreased detectivity at $D_{th}^{*} = 4 \times 10^{12}$–$8 \times 10^{12}$ Jones over the same spectral range.

Two contributing factors are responsible for the changes in D_{th}^{*}. First, the reduction in the responsivity R directly translates into a decreased value of D_{th}^{*}, which is specifically the case at longer wavelengths, where this reduction is most significant. Second, the increase in the dark current density, which was observed and discussed with regards to the *LDR*, plays also an important role in the changes related to the detectivity D_{th}^{*}, although its

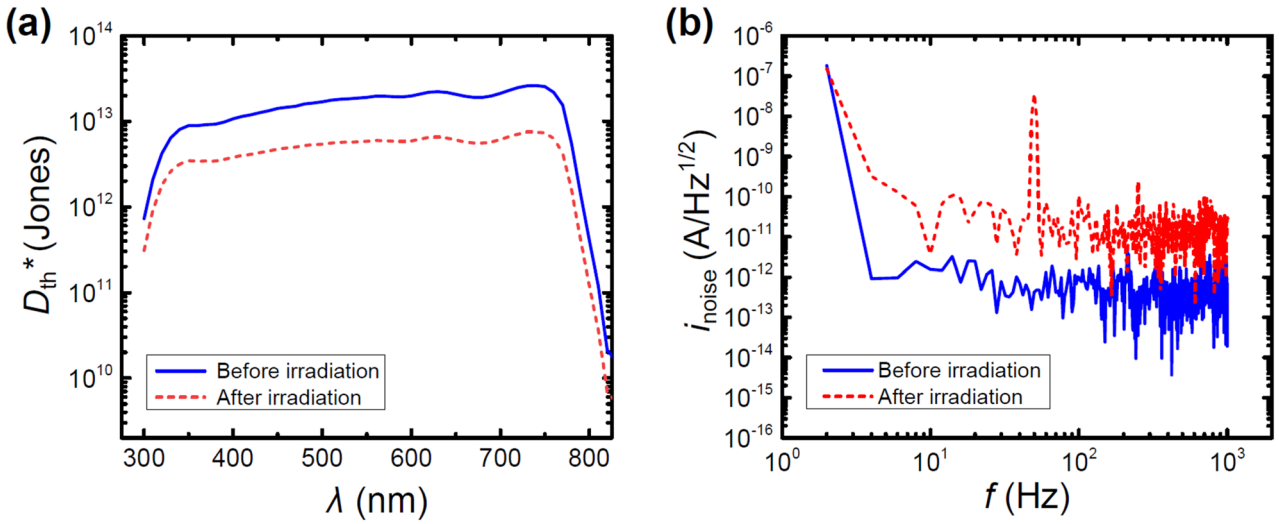

Figure 5. (**a**) Spectral dependence of the detectivity limited by Johnson noise and (**b**) current noise of the tested devices before and after proton irradiation.

contribution is less pronounced due to the fact that it is attenuated via a square root. However, it likely is the most important factor for the reduction of D_{th}^{*} at shorter wavelengths, since the changes in the responsivity R in this spectral region are less significant.

Furthermore, the noise current spectral density i_{noise} is another important, experimentally available characteristic that is used to properly describe PDs (cf. ESI)[19]. It can be observed that the current noise density of the tested devices increases by roughly two orders of magnitude upon proton irradiation over the entire tested frequency range (cf. Fig. 5). Furthermore, the noise current spectral density of the PDs was then utilized to determine the noise equivalent power (NEP) and specific detectivity (D^{*}); the first quantifies the sensitivity of PDs with regards to the signal power resulting in a unity signal-to-noise ratio at the bandwidth of 1 Hz, whereas the second is the detectivity, if all potential sources of current noise are taken into consideration (cf. ESI). Moreover, the applicable bandwidth of a photodetector can be evaluated via its cutoff frequency $f_{-3\,dB}$, which is defined as the frequency at which the output of a PD is attenuated to − 3 dB (70.8%) of the original amplitude. The time dependent photoresponse of the PDs was investigated to obtain the corresponding normalized response, which in turn allows to determine the cutoff frequency $f_{-3\,dB}$ (cf. Figs. S7–S9). Interestingly, it was revealed that the cutoff frequency for the tested PDs before and after proton irradiation are virtually identical at $f_{-3\,dB} = 180$ kHz, which likely result from the limiting RC time constant. Nonetheless, the aforementioned values indicate comparable behavior between the tested PDs before and after proton irradiation up to the RC limit. In addition, the rise times decreased after irradiation, while only small changes in the fall times of the PDs before and after proton irradiation were observed (cf. Table 3 and Fig. S10).

Overall, the assessed devices demonstrate promising characteristics as PDs both prior to and following proton irradiation, particularly when functioning in a self-powered mode. Although proton irradiation led to a decrease in both responsivity R and detectivity D_{th}^{*}, the linear dynamic range LDR exhibited virtually no alteration.

Conclusion

In conclusion, MAPI-based perovskite devices fabricated through vacuum deposition were exposed to proton irradiation, resulting in changes of the electrical and optical properties. The studied solar cells demonstrated efficiencies ranking among the highest reported in the literature for this specific irradiation treatment. A thorough analysis revealed that the primary factors influencing the observed changes in performance as solar cells were a significant reduction in shunt resistance R_{sh} and, to a lesser extent, an increase in series resistance R_s. Some changes in recombination dynamics were observed as well, although the impact on device performance is less pronounced as the aforementioned two loss processes. Furthermore, the devices maintained promising photodetector characteristics both before and after proton irradiation, especially when operated in a self-powered mode without a reverse bias. Although a decrease in responsivity R and detectivity D_{th}^{*} was noted after proton irradiation, the linear dynamic range LDR remained largely unaffected. These results contribute valuable insights

Sample	R_{max} (A/W)	$D_{th}{}^{*}_{max}$ (Jones)	$LDR_{0.0\,V}$ (dB)	$LDR_{-0.1\,V}$ (dB)	$LDR_{-0.5\,V}$ (dB)	t_{rise} (µs)	t_{fall} (µs)
Before irradiation	0.48	3×10^{13}	124	124	99	7.2	3.4
After irradiation	0.35	8×10^{12}	118	99	75	4.1	3.8

Table 3. Photodiode parameters obtained for the tested devices before and after proton irradiation.

into the impact of ionizing radiation on perovskite devices manufactured via vacuum deposition and underscore their potential for applications in radiation-prone environments.

The degradation mechanism during proton irradiation likely involves the breaking of covalent bonds within the molecules of the perovskite active layer. The breaking of bonds results in the formation of localized defective states within the band gap. The location of these defective states within the band gap determines whether they act as effective recombination centres or charge traps. The presence of these centres has a detrimental effect on photovoltaic performance. The observed increase in series resistance and decrease in fill factor can be attributed to the occurrence of damage to the ETL/HTL and/or electrodes.

The present study is primarily concerned with proton-induced alterations in the physical properties of fully evaporated perovskite solar cells and photodiodes. Although we make certain assumptions based on the existing knowledge of radiation-induced degradation mechanisms in perovskite optoelectronic devices, further comprehensive and multifaceted material characterization of all functional layers that make up the device stack is required to unravel the exact degradation mechanisms in proton-irradiated perovskite optoelectronic devices.

Data availability

The materials and data that support the findings of this study are available from the corresponding authors on request.

Received: 11 April 2024; Accepted: 12 July 2024
Published online: 20 July 2024

References

1. Zhang, H., Pfeifer, L., Zakeeruddin, S. M., Chu, J. & Grätzel, M. Tailoring passivators for highly efficient and stable perovskite solar cells. *Nat. Rev. Chem.* **7**, 632–652 (2023).
2. Gao, H. *et al.* Recent progress in all-small-molecule organic solar cells. *Small* **19**, 2205594 (2023).
3. Li, S., Li, Z., Wan, X. & Chen, Y. Recent progress in flexible organic solar cells. *eScience* **3**, 100085 (2023).
4. Li, X. *et al.* Progress and challenges toward effective flexible perovskite solar cells. *Nano-Micro Lett.* **15**, 206 (2023).
5. NREL. *Best Research-Cell Efficiency Chart*. https://www.nrel.gov/pv/cell-efficiency.html (2024).
6. Kim, S.-W. *et al.* Reducing humidity dependency of ambient-air-processed wide-bandgap inverted perovskite solar cells. *ACS Energy Lett.* **8**, 4777–4781 (2023).
7. Roß, M. *et al.* Co-evaporated formamidinium lead iodide based perovskites with 1000 h constant stability for fully textured monolithic perovskite/silicon tandem solar cells. *Adv. Energy Mater.* **11**, 2101460 (2021).
8. Jošt, M. *et al.* Subcell operation and long-term stability analysis of perovskite-based tandem solar cells using a bichromatic light emitting diode light source. *Sol. RRL* **5**, 2100311 (2021).
9. Jiang, Y. *et al.* Negligible-Pb-waste and upscalable perovskite deposition technology for high-operational-stability perovskite solar modules. *Adv. Energy Mater.* **9**, 1803047 (2019).
10. Ahmed Chowdhury, T. *et al.* Stability of perovskite solar cells: Issues and prospects. *RSC Adv.* **13**, 1787–1810 (2023).
11. Bush, K. A. *et al.* Compositional engineering for efficient wide band gap perovskites with improved stability to photoinduced phase segregation. *ACS Energy Lett.* **3**, 428–435 (2018).
12. Tan, L. *et al.* Combined vacuum evaporation and solution process for high-efficiency large-area perovskite solar cells with exceptional reproducibility. *Adv. Mater.* **35**, 2205027 (2023).
13. Sun, C., Jiang, Y., Wei, K. & Yuan, M. Perovskite light-emitting diodes toward commercial full-colour displays: Progress and key technical obstacles. *Light Adv. Manuf.* **4**, 272–291 (2023).
14. Wu, W. *et al.* Recent progress on wavelength-selective perovskite photodetectors for image sensing. *Small Methods* **7**, 2201499 (2023).
15. Zhang, X. *et al.* Review on flexible perovskite photodetector: Processing and applications. *Front. Mech. Eng.* **18**, 33 (2023).
16. Lee, J. *et al.* Side-chain engineering of nonfullerene acceptors for near-infrared organic photodetectors and photovoltaics. *ACS Energy Lett.* **4**, 1401–1409 (2019).
17. Huang, J. *et al.* A high-performance solution-processed organic photodetector for near-infrared sensing. *Adv. Mater.* **32**, 1906027 (2020).
18. Ozerova, V. V. *et al.* Exploring the limits: Degradation behavior of lead halide perovskite films under exposure to ultrahigh doses of γ rays of up to 10 MGy. *J. Phys. Chem. Lett.* **14**, 743–749 (2023).
19. Solovan, M. M. *et al.* Extreme radiation resistance of self-powered high-performance $Cs_{0.04}Rb_{0.04}(FA_{0.65}MA_{0.35})_{0.92}Pb(I_{0.85}Br_{0.14}Cl_{0.01})_3$ perovskite photodiodes. *Adv. Opt. Mater.* **11**, 2203001 (2023).
20. Parkhomenko, H. P. *et al.* Self-healing of proton-irradiated organic photodiodes and photovoltaics. *Adv. Energy Mater.* **13**, 2301696 (2023).
21. Xiong, G. *et al.* Radiation hardness and abnormal photoresponse dynamics of the CH3NH3PbI3 perovskite photodetector. *J. Mater. Chem. C* **9**, 2095–2105 (2021).
22. Abzieher, T. *et al.* Efficient all-evaporated pin-perovskite solar cells: A promising approach toward industrial large-scale fabrication. *IEEE J. Photovolt.* **9**, 1249–1257 (2019).
23. Ritzer, D. B. *et al.* Upscaling of perovskite solar modules: The synergy of fully evaporated layer fabrication and all-laser-scribed interconnections. *Prog. Photovolt. Res. Appl.* **30**, 360–373 (2022).
24. Lang, F. *et al.* Methylammonium-free co-evaporated perovskite absorbers with high radiation and UV tolerance: An option for in-space manufacturing of space-PV?. *RSC Adv.* **13**, 21138–21145 (2023).
25. Li, P. *et al.* Tolerance of perovskite solar cells under proton and electron irradiation. *Materials* **15**, 1393 (2022).
26. Colenbrander, T. *et al.* Low-intensity low-temperature analysis of perovskite solar cells for deep space applications. *Energy Adv.* **2**, 298–307 (2023).
27. Lang, F. *et al.* Proton-radiation tolerant all-perovskite multijunction solar cells. *Adv. Energy Mater.* **11**, 2102246 (2021).
28. Scolese, C. J. *Low Earth Orbit Spacecraft Charging Design Handbook* (2007).
29. Squire, T. *U.S. Standard Atmosphere, 1976* (2000).
30. AVS Reference Guide—Glossary. https://web.archive.org/web/20060304160701/http://www.aip.org/avsguide/refguide/glossary.html#v (2006).
31. Lang, F. *et al.* Efficient minority carrier detrapping mediating the radiation hardness of triple-cation perovskite solar cells under proton irradiation. *Energy Environ. Sci.* **12**, 1634–1647 (2019).
32. Billur, C. A., Şahin, G., Güneri, E., Saatçi, B. & Soylu, M. Ç. The effect of films thickness on structural and optical properties of amorphous Sn_2O thin films deposited by ink jet printing method. *J. Mol. Struct.* **1219**, 128577 (2020).

33. Huang, J. H. *et al.* Direct conversion of $CH_3NH_3PbI_3$ from electrodeposited PbO for highly efficient planar perovskite solar cells. *Sci. Rep.* **5**, 1–8 (2015).
34. Kirmani, A. R. *et al.* Countdown to perovskite space launch: Guidelines to performing relevant radiation-hardness experiments. *Joule* **6**, 1015–1031 (2022).
35. Solovan, M. M. *et al.* A high-detectivity, fast-response, and radiation-resistant TiN/CdZnTe heterojunction photodiode. *Adv. Opt. Mater.* **11**, 2202028 (2023).
36. Parkhomenko, H. P. *et al.* Impact of a short-pulse high-intense proton irradiation on high-performance perovskite solar cells. *Adv. Funct. Mater.* **34**, 2310404 (2024).
37. Sze, S. M., Li, Y. & Ng, K. K. *Physics of Semiconductor Devices* (Wiley, 2021).
38. Nelson, J. A. *The Physics Of Solar Cells* (World Scientific Publishing Company, 2003).
39. Hong, J., Kim, H. & Hwang, I. Aging-induced light-soaking effects and open-circuit voltage hysteretic behavior of inverted perovskite solar cells incorporating a hole transport metal halide layer via morphology-dependent inflow of iodide ions. *J. Mater. Chem. C* **7**, 1173–1181 (2019).
40. Gupta, V., Lucarelli, G., Castro-Hermosa, S., Brown, T. & Ottavi, M. Investigation of hysteresis in hole transport layer free metal halide perovskites cells under dark conditions. *Nanotechnology* **31**, 445201 (2020).
41. Brus, V. V. *et al.* Defect dynamics in proton irradiated $CH_3NH_3PbI_3$ perovskite solar cells. *Adv. Electron. Mater.* **3**, 1600438 (2017).
42. Glowienka, D. & Galagan, Y. Light intensity analysis of photovoltaic parameters for perovskite solar cells. *Adv. Mater.* **34**, 2105920 (2022).
43. Vollbrecht, J. *et al.* Design of narrow bandgap non-fullerene acceptors for photovoltaic applications and investigation of non-geminate recombination dynamics. *J. Mater. Chem. C* **8**, 15175–15182 (2020).
44. Brus, V. V. Light dependent open-circuit voltage of organic bulk heterojunction solar cells in the presence of surface recombination. *Org. Electron.* **29**, 1–6 (2016).
45. Vollbrecht, J. & Brus, V. V. On the recombination order of surface recombination under open circuit conditions. *Org. Electron.* **86**, 105905 (2020).
46. Vollbrecht, J. & Brus, V. V. Effects of recombination order on open-circuit voltage decay measurements of organic and perovskite solar cells. *Energies* **14**, 4800 (2021).
47. Proctor, C. M., Kuik, M. & Nguyen, T.-Q. Charge carrier recombination in organic solar cells. *Prog. Polym. Sci.* **38**, 1941–1960 (2013).
48. Vollbrecht, J. *et al.* Quantifying the nongeminate recombination dynamics in nonfullerene bulk heterojunction organic solar cells. *Adv. Energy Mater.* **9**, 1901438 (2019).
49. Schopp, N. *et al.* Unraveling device physics of dilute-donor narrow-bandgap organic solar cells with highly transparent active layers. *Adv. Mater.* **34**, 2203796 (2022).
50. Brus, V. V. *et al.* Temperature and light modulated open-circuit voltage in nonfullerene organic solar cells with different effective bandgaps. *Adv. Energy Mater.* **11**, 2003091 (2021).
51. Zaban, A., Greenshtein, M. & Bisquert, J. Determination of the electron lifetime in nanocrystalline dye solar cells by open-circuit voltage decay measurements. *ChemPhysChem* **4**, 859–864 (2003).
52. Vollbrecht, J. & Brus, V. V. On charge carrier density in organic solar cells obtained via capacitance spectroscopy. *Adv. Electron. Mater.* **6**, 2000517 (2020).
53. Brus, V. V., Proctor, C. M., Ran, N. A. & Nguyen, T.-Q. Capacitance spectroscopy for quantifying recombination losses in non-fullerene small-molecule bulk heterojunction solar cells. *Adv. Energy Mater.* **6**, 1502250 (2016).
54. Vollbrecht, J. *et al.* Determination of the charge carrier density in organic solar cells: A tutorial. *J. Appl. Phys.* **131**, 221101 (2022).
55. Potscavage, W. J. Jr., Sharma, A. & Kippelen, B. Critical interfaces in organic solar cells and their influence on the open-circuit voltage. *Acc. Chem. Res.* **42**, 1758–1767 (2009).
56. Zhou, X. *et al.* Different morphology dependence for efficient indoor organic photovoltaics: The role of the leakage current and recombination losses. *ACS Appl. Mater. Interfaces* **13**, 44604–44614 (2021).
57. Tvingstedt, K. *et al.* Removing leakage and surface recombination in planar perovskite solar cells. *ACS Energy Lett.* **2**, 424–430 (2017).
58. Proctor, C. M. & Nguyen, T.-Q. Effect of leakage current and shunt resistance on the light intensity dependence of organic solar cells. *Appl. Phys. Lett.* **106**, 083301 (2015).
59. De Rossi, F. *et al.* Neutron irradiated perovskite films and solar cells on PET substrates. *Nano Energy* **93**, 106879 (2022).
60. Yerlanuly, Y. *et al.* Achieving stable photodiode characteristics under ionizing radiation with a self-adaptive nanostructured heterojunction CNWs/CdZnTe. *Carbon* **215**, 118488 (2023).

Acknowledgements

This work is supported by the Collaborative Research Program Grant of Nazarbayev University Grant No. 11022021CRP1505 and the Faculty-Development Competitive Research Program Grant of Nazarbayev University Grant No. 11022021FD2915. M.K. acknowledges funding from the Ministry of Education and Science of the Republic of Kazakhstan Grant No. AP13067604. This work was funded by the state of Lower Saxony and the Federal Ministry for Economic Affairs and Climate Action (BMWK) under grant numbers FKZ 03EE10178 (P3T) and FKZ 03EE1098B (2PowerPero).

Author contributions

All measurement and device characterization was done mostly by H.P.P., A.I.M., and J.V. The proton irradiation was performed by M.K. The first draft of the manuscript was written by J.V. and H.P.P. V.V.B. supervised the project and helped with writing the manuscript. M.D. and S.J.W. initially optimized the active layer evaporation process. J.S. and M.C.T. deposited the transport and active layers. V.S. deposited the electrodes and performed initial characterization.

Competing interests

The authors declare no competing interests.

Additional information

Supplementary Information The online version contains supplementary material available at https://doi.org/10.1038/s41598-024-67541-5.

Correspondence and requests for materials should be addressed to J.V. or V.V.B.